# Global Structure of Magnetorotationally Turbulent Protoplanetary Discs

M. Flaig, <sup>1</sup> Patrick Ruoff<sup>2</sup>, W. Kley<sup>1</sup> and R. Kissmann<sup>3</sup>

<sup>1</sup> Institut für Astronomie & Astrophysik, Universität Tübingen, Auf der Morgenstelle 10, 72076 Tübingen, Germany

- <sup>2</sup> Karlsruhe Institute of Technology, Institut f¨ur Anthropomatik, Adenauerring 2, 76131 Karlsruhe, Germany
- <sup>3</sup> Institut f¨ur Astro- und Teilchenphysik, Universit¨at Innsbruck, Technikerstraße 25/8, 6020 Innsbruck, Austria

Accepted ??. Received ??; in original form ??

#### ABSTRACT

The aim of the present paper is to investigate the spatial structure of a protoplanetary disc whose dynamics is governed by magnetorotational turbulence. We perform a series of local 3D chemo-radiative MHD simulations located at different radii of a disc which is twice as massive as the standard minimum mass solar nebula of Hayashi (1981). The ionisation state of the disc is calculated by including collisional ionisation, stellar X-rays, cosmic rays and the decay of radionuclides as ionisation sources, and by solving a simplified chemical network which includes the effect of the absorption of free charges by \(\mu\)m-sized dust grains. In the region where the ionisation is too low to assure good coupling between matter and magnetic fields, a non-turbulent central "dead zone" forms, which ranges approximately from a distance of 2 AU to 4 AU from the central star. The approach taken in the present work allows for the first time to derive the global spatial structure of a protoplanetary disc from a set of physically realistic numerical simulations.

**Key words:** accretion, accretion discs – planetary systems:protoplanetary discs – turbulence – instabilities – magnetic fields – MHD – radiative transfer

# INTRODUCTION

According to the present understanding, the process of planet formation takes place in protoplanetary discs, which are accretion discs around young, solar-type stars of the T Tauri class. Obtaining knowledge about the physical conditions in protoplanetary discs is therefore of essential importance for developing viable theories of how planets may form.

One of the most intriguing fact about protoplanetary discs is their rather short lifetime of only about 10 million years (Hartmann et al. 1998). The big question is: How can the matter in the disc get rid of its angular momentum in such a short time-scale? The most likely explanation for this is hydromagnetic turbulence initiated by the magnetorotational instability (MRI), a process which was introduced into the context of accretion disc physics by Balbus & Hawley (1991). Numerical simulations show that magnetorotational turbulence leads to fast outward angular momentum transport that can explain the high accretion rates observed for protoplanetary discs (King et al. 2007). However, the MRI will work properly only if there is good coupling between matter and magnetic fields. Since protoplanetary discs are cool objects, with temperatures in the range of several hundred down to a few tens of Kelvin in most parts of the disc, this is a critical issue.

Where in the disc the MRI is active, and where not, does depend on the value of the ionisation level there. While in the hot, inner regions (at a distance  $R < 1 \,\mathrm{AU}$  from the central star) collisional ionisation suffices to provide good coupling, this is no longer true in the cooler regions further away from the star. There, the disc has to rely on other ionisation sources, like the decay of radionuclides, cosmic rays and X-rays, which are emitted from the corona of the central star. In the planet-forming region, at distances of several AU from the star, the density is so high that neither the Xrays nor the cosmic rays are able to reach the midplane of the disc, leading to a poorly ionised, non-turbulent central "dead zone" (Gammie 1996; Armitage 2011). At these intermediate distances, only the upper layers of the disc are expected to be turbulent and to still provide a small amount of angular momentum transport. In the outer regions, the surface density is low enough for the X-rays to penetrate the whole disc column, so the midplane becomes turbulent again.

While analytical calculations like in Gammie (1996) or simplified 1+1D models like the one developed in Kretke & Lin (2010) can already provide useful models for the structure of protoplanetary discs, the definite answers on the questions of the size of the dead zone and the strength of the angular momentum transport in the disc can only come from numerical simulations. At the present stage it seems very difficult to perform global simulations including realistic physics due to the large computational cost and the numerical complexity (see Fromang & Nelson 2006, 2009; Dzyurkevich et al. 2010; Flock et al. 2011, for examples of global protoplanetary disc simulations). On the other hand, the simpler local simulations, which model only a small part of the disc, do already at the present time allow for the inclusion of additional physics like radiation transport and disc chemistry (Flaig et al. 2010; Hirose & Turner 2011).

In the present paper, we investigate the spatial structure of a protoplanetary disc by performing a series of local 3D magnetohydrodynamical simulations located at different radii, including both radiation transport and the effect of a finite Ohmic resistivity. We choose optimistic physical parameters in order to obtain a small dead zone that fits inside the domain that is simulated. Using this method, we are able to obtain a comprehensive picture of both the vertical and the radial structure of a magnetorotationally turbulent protoplanetary disc.

It should be noted that apart from Ohmic resistivity, ambipolar diffusion might also reduce the saturation level of the MRI. The strength of this effect depends on the value of the neutral-ion collision frequency (see, for example, Bai & Stone 2011). In the fully turbulent regions of our model, the ratio of collision frequency to orbital frequency is  $\gtrsim 100$ , suggesting that in these regions, the saturation level would not be strongly affected by ambipolar diffusion.

The plan of our paper is as follows: In Sec. 2 we describe our physical model and the numerical setup. Sec. 3 presents the results of the numerical simulations and draws connections with astrophysical observations. In Sec. 4, we conclude.

## 2 MODEL SETUP

Our basic setup is very similar to that of the radiative protoplanetary disc simulations described in Flaig et al. (2010). The simulations take place in the so-called stratified local shearing box, which is a rectangular box that covers the full vertical height of the disc but has only a small radial and azimuthal extent. This allows the use of local Cartesian coordinates (x, y, z), where x corresponds to the radial, y to the azimuthal and z to the vertical direction, respectively (for more information on the shearing box setup, see Hawley et al. 1995; Stone et al. 1996; Stone & Gardiner 2010). At the vertical boundaries, outflow boundary conditions are applied, that allow matter and radiation to escape from the disc (see Flaig et al. 2010).

The disc gas is described by the equations of magnetohydrodynamics, where we include radiation transport in the one-temperature flux-limited diffusion approximation (Flaig et al. 2010) as well as the effect of a finite Ohmic resistivity. The physical equations are then given by

$$\begin{split} \frac{\partial \rho}{\partial t} + \nabla \cdot (\rho \boldsymbol{v}) &= 0, \\ \frac{\partial (\rho \boldsymbol{v})}{\partial t} + \nabla \cdot \left[ \rho \boldsymbol{v} \boldsymbol{v} + p_{\text{tot}} \mathsf{I} - \frac{\boldsymbol{B} \boldsymbol{B}}{4\pi} \right] &= \boldsymbol{f}_{\text{ext}}, \\ \frac{\partial \boldsymbol{B}}{\partial t} - \nabla \times (\boldsymbol{v} \times \boldsymbol{B} - \eta \nabla \times \boldsymbol{B}) &= 0, \\ \frac{\partial e_{\text{tot}}}{\partial t} + \nabla \cdot \left[ (e_{\text{tot}} + p_{\text{tot}}) \, \boldsymbol{v} - \frac{(\boldsymbol{v} \cdot \boldsymbol{B}) \boldsymbol{B}}{\mu_0} + \frac{\eta}{\mu_0^2} \nabla \times \boldsymbol{B} \times \boldsymbol{B} \right], \\ &= \boldsymbol{f}_{\text{ext}} \cdot \boldsymbol{v} - \nabla \cdot \boldsymbol{F}; \end{split}$$

with the total energy  $e_{\rm tot}=p/(\gamma-1)+\rho v^2/2+B^2/2\mu_0$ , the total pressure  $p_{\rm tot}=p+B^2/2\mu_0$ , and

$$\mathbf{f}_{\text{ext}} = -2\rho\Omega\hat{\mathbf{z}} \times \mathbf{v} + 3\rho\Omega^2 x\,\hat{\mathbf{x}} - \rho\Omega^2 z\,\hat{\mathbf{z}} \tag{1}$$

denotes the source terms arising in the local shearing box frame (Flaig et al. 2010), with  $\Omega$  the local orbital frequency. The radiation flux is given by  $\mathbf{F} = -(\lambda c/\kappa\rho)\nabla aT^4$ . The use of the flux-limiter  $\lambda$  (for which we use the form suggested by Levermore & Pomraning 1981) makes the radiation transport method applicable also to optically thin regions.

The above equations are solved using a conservative finite volume scheme. The scheme employs the HLLD Riemann solver of Miyoshi & Kusano (2006), which yields a high effective resolution at moderate computational cost.

The value of the resistivity  $\eta$  is calculated by including various ionisation source and by solving a simplified chemical network. As in Hirose & Turner (2011), the values for the resistivity are read from a precomputed table. The value of the resistivity depends on the density, the temperature and the local ionisation rate due to X-rays, cosmic rays and the decay of radionuclides. We now describe the prescription according to which the resistivity is calculated.

## 2.1 Ionisation sources

## 2.1.1 Collisional ionisation

In the hot, inner region inside 1 AU, collisional ionisation is the dominant ionisation source. The ionisation level arising from this process is calculated using the Saha equation, which is given by

$$x_{\rm e} = \frac{n_{\rm e}}{n_{\rm n}} = 6.47 \cdot 10^{-13} \left(\frac{T}{10^3}\right)^{\frac{3}{4}} \times \left(\frac{2.4 \cdot 10^{15}}{n_{\rm n}}\right)^{\frac{1}{2}} \frac{\exp(-25188/T)}{1.15 \cdot 10^{-11}}, \quad (2)$$

where  $n_{\rm e}$  and  $n_{\rm n}$  are the electron and neutral number densities in cm<sup>-3</sup>, respectively, T is the temperature given in Kelvin and we have assumed a potassium abundance of  $10^{-7}$  (see, for example Fromang et al. 2002).

## 2.1.2 Stellar X-rays

In the region where collisional ionisation is low, stellar X-rays are the dominant ionisation source. For the ionisation rate due to X-rays, we use the formula as given by Turner

& Sano (2008),

$$\zeta_{\rm XR}(R,z) = 2.6 \cdot 10^{-15} \,\mathrm{s}^{-1} \left(\frac{R}{1 \,\mathrm{AU}}\right)^{-2} \left(\frac{L_{\rm XR}}{2 \cdot 10^{30} \,\mathrm{erg} \,\mathrm{s}^{-1}}\right) \\
\times \left\{ \exp\left(\frac{-\Sigma^{+}(R,z)}{8 \,\mathrm{g} \,\mathrm{cm}^{-2}}\right) + \left(\frac{-\Sigma^{-}(R,z)}{8 \,\mathrm{g} \,\mathrm{cm}^{-2}}\right) \right\}, \quad (3)$$

where  $\Sigma^{\pm}(R, z)$  are the column densities at radius R above and below a given point z,

$$\Sigma^{\pm}(R,z) = \pm \int_{z}^{\pm \infty} \rho(R,z') \,dz', \tag{4}$$

and  $L_{\rm XR}$  is the stellar X-ray luminosity which we take as

$$L_{XR} = 2 \cdot 10^{31}. (5)$$

Although this is a rather optimistic value, it is still inside the usual range of  $10^{29}-10^{32}\,\mathrm{erg\,s^{-1}}$  for the X-ray luminosities observed for young stellar objects.

### 2.1.3 Cosmic rays

Another possibly important ionisation source are cosmic rays, i.e. highly energetic particles from the interstellar medium that hit the disc. If these particles can reach the interior of the disc, their contribution is given by (Umebayashi & Nakano 2009)

$$\zeta_{\rm CR}(R,z) = \frac{\zeta_{\rm CR,0}}{2} \left\{ \exp\left(-\frac{\Sigma^{+}(R,z)}{\chi_{\rm CR}}\right) \left[1 + \left(\frac{\Sigma^{+}(R,z)}{\chi_{\rm CR}}\right)^{\frac{3}{4}}\right]^{-\frac{4}{3}} + \exp\left(-\frac{\Sigma^{-}(R,z)}{\chi_{\rm CR}}\right) \left[1 + \left(\frac{\Sigma^{-}(R,z)}{\chi_{\rm CR}}\right)^{\frac{3}{4}}\right]^{-\frac{4}{3}} \right\}, \quad (6)$$

where  $\zeta_{\rm CR,0}$  is set to the cosmic ray ionisation rate in the interstellar medium,  $\zeta_{\rm CR,0}=10^{-17}\,{\rm s}^{-1}$ , and  $\chi_{\rm CR}=96.0\,{\rm g\,cm}^{-2}$ .

# 2.1.4 Decay of radionuclides

Finally, we also include the ionisation arising from the decay of radionuclides. Long-lived radionuclides provide a background ionisation level of about  $10^{-22}\,\mathrm{s}^{-1}$ , where the dominant contribution is due to  $^{40}\mathrm{K}$ . This rate can be significantly increased if one includes the effect of short-lived radionuclides, which are no more present in the solar system. The most important contribution comes from the decay of  $^{26}\mathrm{Al}$ , which yields an ionisation rate of  $\zeta_{\mathrm{RA}}=9.2\cdot10^{-20}\,\mathrm{s}^{-1}$  based on the mean interstellar abundance and eight times this value for the projected abundance of the young solar system, which is based on the ratio of different aluminum isotopes found in CAIs in meteorites (Umebayashi & Nakano 2009). Here we adopt an ionisation rate of  $\zeta_{\mathrm{RA}}=7\cdot10^{-19}\,\mathrm{s}^{-1}$ .

#### 2.2 Chemical network

In the region where collisional ionisation is ineffective, the ionisation state of the disc gas is determined by a balance

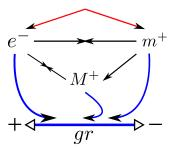


Figure 1. Schematic diagram of the charge-transfer reactions in the ODD network. The symbols m, M and gr denote the generalised molecule species (i.e. mainly H<sub>2</sub>), the generalised metal species (mainly K) and the dust grains, respectively. The red arrows denote the ionisation of molecules, the black arrows denote the recombination and charge transfer reactions involving only molecules and metals, while the blue arrows denote the absorbtion of charged particles on the surface of dust grains.

between ionisation due to the ionisation sources discussed above and recombination of free charges inside the gas. We use the extended Oppenheimer-Dalgarno network of Ilgner & Nelson (2006), which approximates the gas-phase chemistry by a generalized molecule species m and metal species M, extended by the introduction of spherical dust grains which have a grain mass density of  $\rho_{\rm gr}=3~{\rm g\,cm^{-3}}$ . This extended network is called the "ODD network" in the following.

The charges of the newly introduced dust grains are tracked in the range from -2 to 2, leading to five new species  ${\rm gr}^{2-}$  to  ${\rm gr}^{2+}$ . Furthermore, two mantle-species are introduced m(gr) and M(gr), which represent molecules and metals frozen out on the grain surfaces, leading to a total number of 12 species.

The reactions among the different species can be found in (Ilgner & Nelson 2006, table 1, 3 and 4) and are graphically illustrated in Fig. 1. (As we are mainly interested in the overall ionisation fraction, only the reactions involving charged particles are shown). The red ionisation reaction and the black charge transfer and recombination reactions are the same as in the Oppenheimer & Dalgarno (1974) network, whereas the reactions involving dust grains are drawn in blue.

The resistivity is calculated from the ionisation fraction according to the usual formula

$$\eta = 234 x_{\rm e} / \sqrt{T}.\tag{7}$$

The main effect of the dust grains is to provide new, indirect recombination paths for electrons: The grains sweep up free electrons, charging up negatively and simultaneously acquire positive charge through charge transfer reactions with metal and molecule ions. Grain-grain charge transfer reactions ensure that oppositely charged grains neutralise themselves resulting in a relatively narrow grain charge distribution. In contrast to the metal ions, which provide a charge reservoir that can only have a significant effect if enough metal is present in the gas, dust grains behave as a kind of catalyst for recombination. It is therefore possible that even tiny amounts of dust grains can change the equilibrium electron fraction significantly.

# 4 M. Flaig et al.

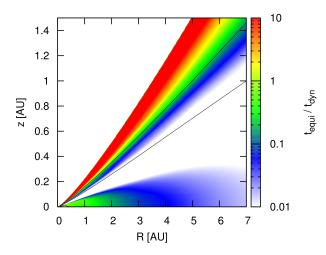


Figure 2. Equilibration time of the ODD network over orbital time as a function of the disc position. The contour lines correspond to a magnetic Reynolds number of  $10^2$  and  $10^4$ , respectively. For further comments, see the text.

### 2.2.1 Equilibration timescale

Fig. 2 shows a plot of the equilibration timescale  $t_{\rm equi}$  over the orbital time  $t_{\rm dyn}=2\pi/\Omega$  for the ODD network, with a grain size of 10 µm, a dust-to-gas ratio of  $10^{-4}$ , a metallicity of  $10^{-10}$  and a disc temperature that varies with the distance R to the central star according to

$$T(R) = 280 (R/AU)^{-1/2} \text{ K.}$$
 (8)

In addition, we also show contour lines for the magnetic Reynolds number defined as

$$Re_{\rm m} \equiv \frac{Hc_{\rm s}}{\eta} = \frac{{c_{\rm s}}^2}{\eta \,\Omega},\tag{9}$$

where  $c_{\rm s}$  is the sound speed and  $H=c_{\rm s}/\Omega$  the pressure scale height. The critical value of Rem for which the transition from the MRI-active to dead occurs, lies somewhere between 10<sup>2</sup> (for the case where the vertical magnetic flux through the disc is non-zero) and 10<sup>4</sup> (for a zero net flux configuration) (see Ilgner & Nelson 2006). As can be seen from Fig. 2, the equilibration timescale mostly stays below the orbital time in the region where the transition from MRI-dead zone to the active zone occurs. This means that turbulent mixing effects can be neglected and the disc gas can be assumed to be in chemical equilibrium all the time. We note that when using a more complex chemical network, the equilibrium timescale is expected to be even shorter, since there are then more recombination channels available (Bai 2011). The chemical equilibrium value for the electron concentration depends only on three parameters, the ionisation rate  $\zeta$ , the temperature T and the total number density of the gas n (assuming a constant dust-to-gas mass ratio and metallicity). This fact allows us to use a previously computed, three dimensional look-up table for the equilibrium resistivity values in our MHD simulation instead of evolving the chemical network during the simulation.

# 2.3 Physical parameters

We take the central star to have one solar mass. Concerning the surface density profile, we assume a disc mass which

Symbol	Value
$M_\star \gamma$	$1 M_{\odot}$ $1.4$
$\mu$	2.35
$L_{ m XR}$	$10^{31}{\rm ergs^{-1}}$
$\zeta_{ m CR}$	$10^{-17}\mathrm{s}^{-1}$
$\zeta_{ m RA}$	$7 \cdot 10^{-19}  \mathrm{s}^{-1}$
$a_{ m gr}$	$10~\mu\mathrm{m}$
$ ho_{ m d}/ ho$	$10^{-4}$
$ ho_{ m gr}$	$3~\mathrm{gcm^{-3}}$
$\dot{M}$	$10^{-10}$
	$M_{\star}$ $\gamma$ $\mu$ $L_{\rm XR}$ $\zeta_{\rm CR}$ $\zeta_{\rm RA}$ $a_{\rm gr}$ $\rho_{\rm d}/\rho$ $\rho_{\rm gr}$

**Table 1.** Summary of basic physical parameters of the physical model. For further comments see the text.

is two times the disc mass as given by the minimum mass solar nebula model of Hayashi (1981), i.e. the surface density profile is given by the formula

$$\Sigma_0 = 3400 \,\mathrm{g \, cm}^{-2} \left(\frac{R}{1 \,\mathrm{AU}}\right)^{-3/2}.$$
 (10)

For this choice of surface density, the disc is to a large part optically thick in the whole radial range spanned by our simulations (see Sec. 3). This means that the one-temperature approximation is well satisfied.

The disc gas is characterised by an adiabatic index of 1.4 and a mean molecular weight of 2.35. In accordance with astrophysical observations, we assume that the dust particles in the disc have grown to a size of several microns, choosing a monodisperse dust grain population with grain size  $a_{\rm gr}=10~\mu{\rm m}$  for the chemical network. We assume that the small dust grains are partly depleted due to grain growth and assume a dust-to-gas ratio of  $\rho_{\rm d}/\rho=10^{-4}$ . The metallicity is taken to be  $M=10^{-10}$ .

As in Flaig et al. (2010), we use the Bell & Lin (1994) opacity model. Since it is based on a dust grain population of smaller size than that used for the chemical network, these two choices are not fully consistent. This fact is, however, not very serious, since the opacity does depend only weakly on the grain size (Pollack et al. 1985) and the opacities in protoplanetary discs are not well known anyway. For this reasons, the use of an improved opacity model is deferred to a future work.

For reference, all the basic physical parameters used in our model are summarised in Table 1.

## 3 SIMULATION RESULTS

We perform seven simulations located at different radii, starting from a distance of 1 AU from the central star up to a distance of 7 AU. The simulations are initialised using the same set of initial conditions as described in Flaig et al. (2010), with an initial constant temperature  $T_0$  (see Table 2), a hydrostatic (Gaussian) density distribution with a surface density according to Eq. (10) and a zero net flux magnetic field that has an initial plasma beta of  $\beta=100$  at the midplane. In terms of the initial pressure scale-height, the box size is one scale-height in the radial direction and 6 scale-heights in the azimuthal direction. The vertical box size is 14 scale-heights for the simulations at R=1 AU and

R [AU]	Box size [AU] $L_x \times L_y \times L_z$	Resolution $n_x \times n_y \times n_z$	Runtime [y]	$T_0$ [K]	$\frac{t_{ m cool}}{t_{ m orb}}$	H [AU]	$\langle\langle T \rangle\rangle$ [K]	$\langle\langle \mathrm{Re_m}\rangle\rangle$	$\langle\langle \alpha \rangle\rangle$
1	0.07 x 0.41 x 0.97	32x64x384	100	1200	42.3	0.07	1537	$1.02\cdot 10^6$	0.038
2	0.11 x 0.67 x 1.35	32x64x256	283	400	29.8	0.09	249.7	441.5	$9.3 \cdot 10^{-5}$
3	0.15 x 0.88 x 1.17	32x64x256	519	200	24.0	0.11	139.0	515.9	0.001
4	0.22x1.35x1.80	32x64x256	800	200	6.5	0.15	122.5	1091.8	0.004
5	0.31x1.89x3.15	32x64x256	1118	200	2.3	0.28	161.8	24903.4	0.013
6	0.36x2.15x3.58	32x64x256	1469	150	6.7	0.34	163.1	17336.4	0.039
7	0.45x2.71x3.61	32x64x256	1851	150	3.3	0.24	54.4	1983.14	0.011

Table 2. Overview of the simulation runs that were performed. Listed are the distance to the central star (first column), the box size (second column), the number of grid cells in each direction (third column), the time in years each simulations has run (fourth column), the initial temperature (fifth column), the initial cooling time in units of the orbital period (sixth column), the final scale height (seventh column), the mean temperature (eighth column), the mean magnetic Reynolds number (ninth column) and the alpha parameter (tenth column). The time-averages for the quantities listed in columns eight to ten have been performed from 40 to 100 orbits.

10 scale-heights for the simulations at R=5 and R=6 AU, while for all other simulations it is 8 scale-heights. The corresponding box sizes as measured in AU can be found in Table 2. The simulations are seeded with small random velocity perturbations of order  $\sim 0.01c_{\rm s}$ , leading to rapid development of the MRI, such that the disc reaches a fully turbulent state already within the first ten orbits (see Fig. 4 later in the paper). Each simulation ran for 100 local orbits. The corresponding runtimes in years are also listed int Table 2.

## 3.1 Time history

### 3.1.1 Thermal equilibrium

In our setup, where we neglect the heating due to the irradiation from the central star, the thermal structure of the disc is determined by a dynamical balance between internal heating<sup>1</sup> and radiative cooling. Estimating the cooling time due to radiative diffusion from the relation

$$t_{\rm cool} = H^2/D_{\rm rad},\tag{11}$$

where the radiative diffusion coefficient  $D_{\rm rad}$  is given by

$$D_{\rm rad} = \frac{4acT^3}{3c_{\rm V}\kappa\rho^2} \tag{12}$$

(Flaig et al. 2010), we expect the simulations to reach thermodynamical equilibrium after a few tens of orbits (see Table 2). The resulting temperature should then be independent of the initial temperature.

In Fig. 3, the temporal evolution of the density-weighted spatially averaged temperature

$$\langle T \rangle_{\rho} = \frac{\int \rho \, T \, \mathrm{d}V}{\int \rho \, \mathrm{d}V} \tag{13}$$

is shown. This plot suggest that the simulations do indeed reach a state of at least approximate thermodynamical equilibrium, with the possible exception of the simulations at

<sup>1</sup> Note that the heating due to the turbulent dissipation of kinetic and magnetic energy is included in this, since by virtue of the conservative nature of the underlying numerical scheme, any loss of kinetic and magnetic energy is automatically captured as gas internal energy (see Flaig et al. 2010).

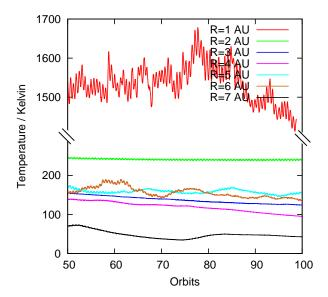


**Figure 3.** Density-weighted temperature as a function of time. Note that the y-axis has been broken in order to include the results from the model at R=1 AU, which has a much higher temperature than the other models.

R=3 and R=4 AU, which show a weak trend to cool during the whole course of the simulation.

The time-averaged values of the temperature found in in the different simulations are listed in Table 2. Especially noticeable is the sharp drop in temperature between the simulations at R=1 and R=2 AU, which is due to the formation of a dead zone (see below).

## 3.1.2 Turbulent activity

We measure the turbulent activity by calculating the r- $\phi$  (or x-y) component of the stress tensor normalised to the gas pressure, the so-called "alpha parameter", according to the following prescription:

$$\langle \alpha \rangle \equiv \frac{\langle T_{xy} \rangle_{\rho}}{\langle p \rangle_{\rho}},\tag{14}$$

where  $T_{xy} = T_{xy}^{\text{Reyn}} + T_{xy}^{\text{Maxw}}$  and  $T_{xy}^{\text{Reyn}}$  and  $T_{xy}^{\text{Maxw}}$  are the Reynolds and Maxwell stresses, which are defined as

$$T_{xy}^{\mathrm{Reyn}} = \rho v_x \, \delta v_y$$
 and  $T_{xy}^{\mathrm{Maxw}} = -B_x B_y / \mu_0$  (15)

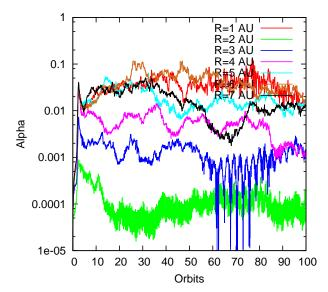


**Figure 4.** Alpha parameter (turbulent stress normalised to gas pressure) as a function of time. For further comments, see the text.

where  $\delta v_y$  is the azimuthal component of the gas velocity with the velocity of the background shear flow subtracted. The quantity  $T_{xy}$  is related to the amount of outward angular momentum transport taking place at a certain location (see, e.g. Balbus 2003).

The time evolution of the alpha parameter is plotted in Fig. 4, the time-averaged values of alpha can be found in Table 2. Within the first ten orbits, all simulations reach a state of saturated turbulence and remain turbulent until the end of the simulation.

The value of alpha drops sharply when going from  $R=1~{\rm AU}$  to  $R=2~{\rm AU}$ , where the ionisation level is very low, since the gas is too cool for collisional ionisation and too thick for either the the X-rays or the cosmic rays too reach the midplane (see Fig. 10 later in the paper). When going further outwards, the ionisation level increases, since there a significant fraction of the cosmic rays is able to penetrate the disc, leading to an increase in the turbulent activity. The simulation at  $R=6~{\rm AU}$  is again fully turbulent, with a mean alpha that is the same as for the simulation at  $R=1~{\rm AU}$ . The stresses found in the poorly ionised models at  $R=2-4~{\rm AU}$  are one to three orders of magnitude smaller than found for the well ionised case.

Turbulence mixes gas and dust and counteracts the force of gravity which causes the dust particles to settle towards the midplane. Based on the levels of turbulence found in our simulations, we can estimate up to which height gas and dust can be considered to be well mixed. We do this by equating the settling time-scale  $t_{\rm s}=1/\Omega^2 t_{\rm d}$  (where  $t_{\rm d}=\rho_{\rm gr}a_{\rm gr}/\rho c_{\rm s}$  is the drag time) with the turbulent mixing time-scale  $t_{\rm m}=H^2/D_{\rm dust}$ . The dust diffusion coefficient  $D_{\rm dust}$  is related to the alpha parameter via the Schmidt number  $S_{\rm c}$  according to  $S_{\rm c}=\alpha c_{\rm s}H/D_{\rm dust}$  (Fromang & Papaloizou 2006). For a density profile in hydrostatic equilibrium,  $\rho(z)=\rho_0\exp(-z^2/2H^2)$ , the height  $z_0$  up to which gas and dust are well mixed then follows from  $t_{\rm s}=t_{\rm m}$  to be

$$\frac{z_0}{H} = \sqrt{-2\ln\frac{\alpha}{S_c}\Omega t_d(z=0)}.$$
 (16)

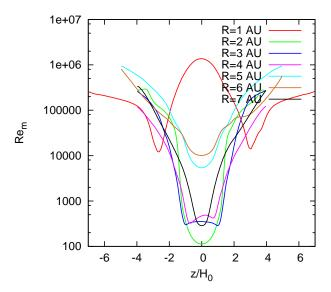


**Figure 5.** Vertical profiles of the mean magnetic Reynolds number, averaged from 60 to 100 orbits. The distance from the midplane is given in units of the initial pressure scale-height  $H_0$ . For further comments, see the text.

Numerical simulations indicate a Schmidt number of order unity (Johansen & Klahr 2005; Turner et al. 2006; Fromang & Papaloizou 2006). Setting  $S_{\rm c}=1$ , and using the initial values for the midplane density and sound speed, as well as the alpha values from Table 2, Eq. (16) predicts  $z_0=2.3H$  for the run at R=2 while for all other runs  $z_0>3H$ . Since the MRI operates mainly within the first three scaleheights (cf. Fig. 6 later in the paper), this means that gas and dust can be considered to be well mixed in the MRI active regions, so the approximation of a constant dust-togas ratio is indeed justified.

#### 3.2 Spatial structure

## 3.2.1 Ionisation level & stress profiles

Concerning the spatial structure of the disc, we first consider the question of how the ionisation level and the turbulent activity vary as a function of position. In Fig. 5, we plot the vertical profile of the magnetic Reynolds number, as defined in Eq. (9).

Judging from the condition that regions with  $Re_m > 10^4$  can be considered sufficiently ionised for the MRI not to be reduced, we can say that the simulations at R=1 and R=6 AU can be considered as ideal. All other simulations contain at least a small zone of insufficient ionisation near the midplane.

Consequently, the vertical stress profiles, which are shown in Fig. 6, are roughly similar for the "ideal" simulations at R=1 and R=6 AU. The simulations at R=5 and R=7 AU exhibit only a small dip in the stress near the midplane, while in the other simulations, the stresses drop noticeably there, forming an extended non-turbulent dead zone ranging from a distance of R=2-4 AU from the central star.

As in the paper of Simon et al. (2011), who also used the HLLD Riemann solver, we do not observe a double peak in the stress profiles of the well ionised simulations at R =

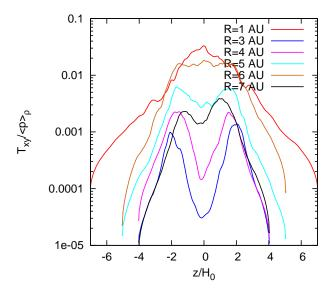


Figure 6. Vertical profiles of the total stress normalised to the mean gas pressure  $\langle p \rangle_{\rho}$ , showing the formation of non-turbulent zones near the midplane due to insufficient ionisation. Averages have been performed from 60 to 100 orbits.

1 and R=6 AU. This is contrary to previous previous stratified simulations like that of Hirose et al. (2009) or Flaig et al. (2010). Since the only major difference in the numerical code as compared to the calculations presented in Flaig et al. (2010) is the change of Riemann solver, it seems that the absence of the double peak profile is indeed due to the use of the HLLD solver.

## 3.2.2 Structure of the magnetic field

Concerning the structure of the magnetic field, we plot snapshots of the magnetic field structure for three different runs in Fig. 7. The left plot shows the magnetic field structure in the fully ideal run at  $R=1\,\mathrm{AU}$ . Within a distance of approximately two to three pressure scale-heights from the midplane, the MRI is fully operational and the magnetic field is highly tangled. Further outwards, the disc becomes magnetically dominated, which leads to a quenching of the MRI, with the magnetic field being predominantly azimuthal. Even further away from the midplane, above four pressure-scale heights, the magnetic field becomes distorted again. The magnetic field structure that we find for the ideal model is very similar to the field structure found by Hirose et al. (2006) (see also Simon et al. 2011).

In the non-ideal runs, the magnetic field structure looks quite different, as one can see from the middle plot of Fig. 7, which shows the magnetic field structure in the very poorly ionised run at R=2 AU. Here the magnetic field is laminar in the region around the midplane, with only the upper layers retaining some level of turbulent activity. This plot can be compared with Hirose & Turner (2011).

Finally, in the right plot of Fig.7, we show a snapshot of the magnetic field for the run at R=5 AU. The magnetic field structure is quite similar to that of the run at R=1 AU, with the difference that the magnetic field near the midplane is more laminar.

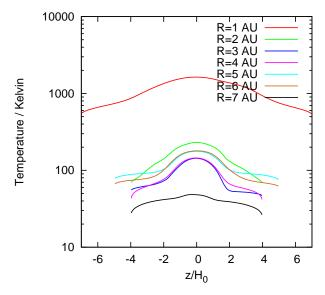


Figure 8. Mean vertical temperature profiles, averaged from 60 to 100 orbits.

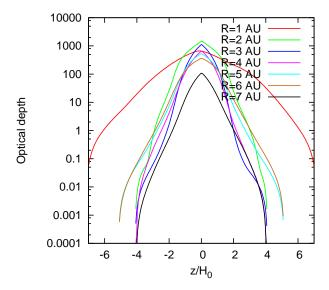


Figure 9. Mean vertical profiles of the optical depth, averaged from 60 to 100 orbits.

#### 3.2.3 Thermal structure

Next, we turn to the question of how the thermal structure of the disc looks like. We show the temperature profiles in Fig. 8. The temperature decreases monotonically with increasing distance from the central star except at the outer edge of the dead zone, where it increases when going from  $R=4~\mathrm{AU}$  to  $R=5~\mathrm{AU}$ , due to the increased turbulent heating.

Vertical profiles of the optical depth are shown in Fig. 9. In all the simulations, the midplane is optically thick, which justifies the use of the one-temperature approximation. Also, the photosphere is located well inside the computational domain for all the simulations.

It is noticeable that the simulations at R=2 and R=3 AU have a larger central optical depth than the simulation at R=1 AU. Also, the optical depth does not change

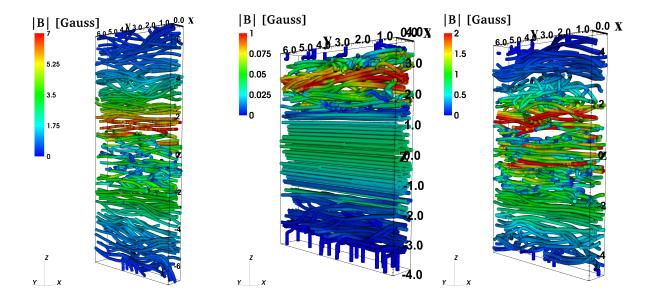


Figure 7. Snapshots of the magnetic field structure for the runs at R = 1 AU (left plot, taken at t = 50 orbits), R = 2 AU (middle plot, taken at t = 90 orbits), and R = 5 AU (right plot, taken at t = 80 orbits). The distances are given in terms of the initial pressure scale-height.

very much for the five simulations in the range from 2 to 6 AU. Both observations can be understood from the fact that these simulations lie in a temperature range where the opacity increases strongly with decreasing temperature (scaling like  $\kappa \propto T^{-7}$  in this region), which balances the effect of the change in surface density on the optical depth.

#### 3.2.4 Global disc structure

By interpolating between the results obtained from the local simulations at different radii, we can calculate time-averaged maps in the R-z plane for the quantities of interest, leading to an axisymmetric model of a protoplanetary disc in steady state, which is derived from physically realistic three-dimensional numerical simulations.

Fig. 10 shows the total ionisation rate due to the stellar X-rays, cosmic rays and the decay of radionuclides. Within the first 3-4 AU, the radionuclides dominate the ionisation rate near the midplane, while outside of 4 AU, the cosmic rays dominate. For the whole radial range considered, the X-rays become dominant only in the upper layers, at distances  $\gtrsim 0.2\text{-}0.3$  AU away from the midplane.

Fig. 11 is intended to give an impression of how the disc looks on average in the quasi steady state obtained in the local simulations presented in this paper. Shown is the density, the location of the photosphere and the magnetosphere as well as the location where the flow becomes supersonic. The average extent of the dead zone is also shown, based on the criterion that the the magnetic Reynolds number be smaller than 1000. The appearance of a second dead zone at  $R=7~{\rm AU}$  is likely an artefact of our particular setup, where we neglect the heating due to the stellar irradiation, leading to an unrealistically low temperature of only  $\sim 50~{\rm K}$  and poor ionisation.

We note that as in the model of Flaig et al. (2010),

which was located at  $R=1~\mathrm{AU}$  with a surface density about six times that of the minimum mass solar nebula, the photosphere lies always inside the magnetically dominated region, although the model presented here is much less massive, and we perform simulations at larger radii. As in the Flaig et al. (2010) model, inside the first 2-3 AU, the turbulence is supersonic at the location of the photosphere, but becomes slightly subsonic there at larger distances from the central star. The conclusion drawn in Flaig et al. (2010) that the MRI can be considered as a possible source for the turbulent line broadening observed in protoplanetary discs, can thus in principle be carried over to models containing dead zones. We note that a recent study (Simon et al. 2011), also finds supersonic velocities above three scale-heights, both for ideal models and models containing a dead zone.

Fig. 12 shows the interpolated mean magnetic field strengths found in the simulations presented in this paper. The field strengths have of course a minimum at the location of the dead zone. Outside of 2 AU, the mean field strengths are almost everywhere below  $\approx 0.2$  G. The field strengths obtained in the present model are probably too low to explain the remnant magnetic fields found in chondritic meteorites, which suggests that a more massive (probably fully active) disc is needed to explain these observations (King & Pringle 2010).

## 4 SUMMARY & CONCLUSION

We have calculated the spatial structure of a magnetorotationally turbulent protoplanetary disc from a series of physically realistic, local three-dimensional numerical simulations. Inside a distance of 1 AU from the central star, the disc gas is sufficiently ionised by collisional ionisation, so the disc midplane is fully turbulent. Between 1 and 2 AU,

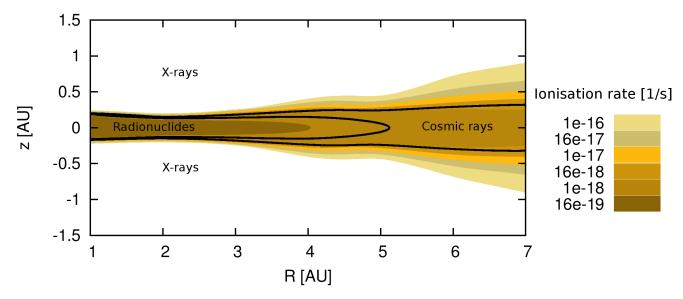


Figure 10. Ionisation rate due to the external ionisation sources. The black line corresponds to the boundary between regions where different ionisation sources dominate.

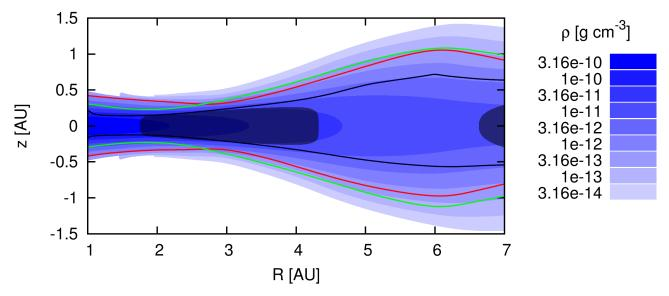


Figure 11. Global spatial structure. Shown is a contour plot of the density. The shaded area corresponds to the region where the magnetic Reynolds number is smaller than 1000. The red line marks the location of the photosphere, the black line corresponds to the the location where magnetic pressure and gas pressure are equal and the green line corresponds to the boundary where the flow starts to become supersonic.

the temperature drops below the threshold of 900 K which is needed for collisional ionisation to be effective, leading to a transition from the fully turbulent state to a state that contains a central non-turbulent dead-zone. When going further outwards, the disc gas becomes thinner, which allows a larger fraction of the stellar X-rays to reach the region around the midplane, leading to a gradual increase in the ionisation level and also the turbulent activity. At R=6 AU, the midplane is again fully turbulent.

The disc gas is heated internally (via turbulent and Ohmic dissipation) with the heating due to the stellar irradiation being neglected. The simulations reach (approximate) thermodynamical equilibrium, except possibly for the simulation located at R=3 and R=4 AU, which continue to cool slowly for the whole course of the simulation. For these two particular runs, the temperature may therefore dependent on the initial conditions, while for all the other simulations, the temperature comes out self-consistently as a result of the balance between internal heating and radiative cooling. Since in most of our simulations the disc gas is for a large part optically thick, we do not expect the stellar irradiation to change the temperature in the interior of the disc drastically, except for the simulation at R=7, where the temperature is indeed unrealistically low (when com-

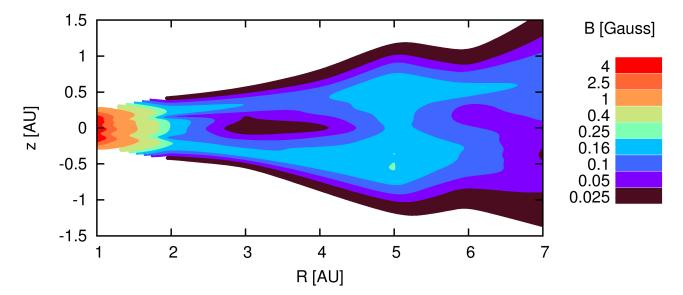


Figure 12. Mean magnetic field strength.

pared, for example, with the passive disc model of Chiang & Goldreich 1997).

It should be noted that the use of the local approximation is a major restriction of the present work, since local simulations cannot capture the full dynamics of a global simulation (see, for example, Sorathia et al. 2011). However, apart from the fact that in a global setup the surface density would change over time, the spatial structure in a global model using the same physics will likely not be dramatically different from the structure coming out in the local framework. Therefore, the approach taken in the present work is a useful first step in deriving the structure of protoplanetary discs from physically realistic numerical simulations.

To summarise, the simulations presented in this work are able to capture all the basic physics that is thought to be important for protoplanetary disc dynamics, and do not suffer from the lack of self-consistency of previous isothermal models. For the first time, it is therefore possible to obtain a picture of the global structure of a magnetorotationally turbulent protoplanetary disc from first-principles numerical simulations.

## ACKNOWLEDGEMENTS

This research has been supported in part by the Deutsche Forschungsgemeinschaft DFG through grant DFG Forschergruppe 759 "The Formation of Planets: The Critical First Growth Phase". Computational resources were provided by the High Performance Computing Cluster of the University of Tübingen. We thank Neal Turner, Mario Flock, Natalia Dzyurkevich and Martin Ilgner for helpful discussions. We also want to thank the anonymous referee for very useful suggestions.

## REFERENCES

Bai X.-N., 2011, ArXiv e-prints

Bai X.-N., Stone J. M., 2011, ApJ, 736, 144

Balbus S., Hawley J., 1991, ApJ, 376, 214

Balbus S. A., 2003, ARA&A, 41, 555

Bell K. R., Lin D. N. C., 1994, ApJ, 427, 987

Brandenburg A., Nordlund A., Stein R. F., Torkelsson U., 1995, ApJ, 446, 741

Chiang E. I., Goldreich P., 1997, ApJ, 490, 368

Dzyurkevich N., Flock M., Turner N. J., Klahr H., Henning T., 2010, A&A, 515, A70+

Flaig M., Kley W., Kissmann R., 2010, MNRAS, 409, 1297 Flock M., Dzyurkevich N., Klahr H., Turner N. J., Henning T., 2011, ApJ, 735, 122

Fromang S., Nelson R. P., 2006, A&A, 457, 343

Fromang S., Nelson R. P., 2009, A&A, 496, 597

Fromang S., Papaloizou J., 2006, A&A, 452, 751

Fromang S., Terquem C., Balbus S. A., 2002, MNRAS, 329,

Gammie C. F., 1996, ApJ, 457, 355

Hartmann L., Calvet N., Gullbring E., D'Alessio P., 1998, ApJ, 495, 385

Hawley J. F., Gammie C. F., Balbus S. A., 1995, ApJ, 440, 742 (HGB)

Hawley J. F., Stone J. M., 1998, ApJ, 501, 758

Hayashi C., 1981, Progress of Theoretical Physics Supplement, 70, 35

Hirose S., Krolik J. H., Blaes O., 2009, ApJ, 691, 16

Hirose S., Krolik J. H., Stone J. M., 2006, ApJ, 640, 901

Hirose S., Turner N. J., 2011, ApJ, 732, L30+

Ilgner M., Nelson R. P., 2006, A&A, 445, 205

Johansen A., Klahr H., 2005, ApJ, 634, 1353

King A. R., Pringle J. E., 2010, MNRAS, 404, 1903

King A. R., Pringle J. E., Livio M., 2007, MNRAS, 376,

Kretke K. A., Lin D. N. C., 2010, ApJ, 721, 1585 Levermore C. D., Pomraning G. C., 1981, ApJ, 248, 321 Miyoshi T., Kusano K., 2006, AGU Fall Meeting Abstracts, pp C275+

Oppenheimer M., Dalgarno A., 1974, ApJ, 192, 29

Pollack J. B., McKay C. P., Christofferson B. M., 1985, Icarus, 64, 471

Sano T., Stone J. M., 2002, ApJ, 577, 534

Simon J., Armitage P., Beckwith K., 2011, ArXiv e-prints Simon J. B., Hawley J. F., Beckwith K., 2011, ApJ, 730, 94

Sorathia K. A., Reynolds C. S., Stone J. M., Beckwith K., 2011, ArXiv e-prints

Stone J. M., Gardiner T. A., 2010, ApJS, 189, 142

Stone J. M., Hawley J. F., Gammie C. F., Balbus S. A., 1996, ApJ, 463, 656

Turner N. J., Carballido A., Sano T., 2010, ApJ, 708, 188

Turner N. J., Sano T., 2008, ApJ, 679, L131

Turner N. J., Willacy K., Bryden G., Yorke H. W., 2006, ApJ, 639, 1218

Umebayashi T., Nakano T., 2009, ApJ, 690, 69